Micromilling of microbarbs for medical implants

Sinan Filiz[a], Luke Xie[a], Lee E. Weiss[b], O.B. Ozdoganlar[a],*

[a]Department of Mechanical Engineering, Carnegie Mellon University, Pittsburgh, PA 15213-3890, USA
[b]Robotics Institute, Carnegie Mellon University, Pittsburgh, PA 15213-3890, USA

Abstract

Successful application of many implantable medical devices often depends on the technique used for attaching the devices to living tissue. Although mechanical attachment techniques that use micro-scale piercing elements are very promising, the fabrication of the micro-scale piercing elements poses considerable challenges. In this paper, the use of the mechanical micromilling process for fabrication of micro-scale piercing elements (*microbarbs*) from biocompatible materials is investigated. Two micro-scale milling tools with custom geometries are used during the fabrication. To gain an understanding of the process conditions on the performance metrics of micromilling forces, surface roughness, and burr formation, a design of experiments study is performed on polymethyl methacrylate (PMMA). The geometric capability of the process is demonstrated by fabricating PMMA microbarbs with different sizes (widths from 68 to 174 μm), edge sharpnesses (60° and 90° included angles), and heights (from 84 to 460 μm). The capability to micromill a variety of biocompatible materials is demonstrated by creating microbarbs from non-biodegradable 304 stainless steel and PMMA, from bioresorbable polylactic acid (PLA), and from a fibrin based plastic. It is concluded that the micromilling process can be used for effectively fabricating arrays of microbarbs.
© 2007 Elsevier Ltd. All rights reserved.

Keywords: Medical device manufacturing; Medical attachment; Mechanical micromachining; Micromilling; Biomedical fabrication; Microbarbs

1. Introduction

Implantable medical devices are widely used for replacing damaged or diseased tissues, performing targeted drug delivery, monitoring and correcting functional abnormalities, and tissue-to-tissue connections [1–3]. Due to functional needs, and biological compatibility considerations, implantable devices are required to be miniature in size and made from biocompatible materials [4,5].

One of the most challenging aspects of application of implantable devices is their attachment to or immobilization within living tissue. Proper functionality, safety, and long-term reliability of implantable devices depend strongly on the attachment technique. Beyond use in current applications attachment components will be critical for various applications; including patches for wound closure on soft tissues, attachment of internal devices for localized drug delivery, soft-tissue reconstruction, vascular anastomosis, general hemostasis, periosteal patches to articular cartilage, orthopedic surgery for fracture repair and prosthetic attachment, and attachment of tissue-engineered scaffolds [4,6–9]. Requirements for an effective attachment technique include minimal damage to the tissue, biocompatibility, mechanical strength, long-term reliability, and rapid deployment, and, in some cases, biodegradability [9,10]. Currently, suturing or gluing are the attachment methods commonly utilized in clinical use.

Microbarb technology, based on micro-scale piercing elements incorporated onto the surfaces of the implantable devices, has been proposed as an alternative attachment method [6,7,11–15]. In comparison to chemical attachment techniques (glues and adhesives) [4,10,16–18], the microbarbs may provide higher attachment strength and increased long-term reliability [8]. In comparison with suturing, attachment to tissues with arrays of microbarbs may be accomplished more quickly and would also facilitate microsurgical procedures [6–8].

*Corresponding author. Tel.: +1 412 268 9890; fax: +1 412 268 3348.
  E-mail address: ozdoganlar@cmu.edu (O.B. Ozdoganlar).

Although mechanical attachment techniques based on micro-scale piercing elements are very promising, manufacturing of these attachment components poses significant challenges. Piercing elements are characterized by micro-scale size complex three-dimensional (3D) geometric features, and arrayed configurations. Furthermore, the attachment components are required to be fabricated from biocompatible materials. Prior work used micro-electro-mechanical systems (MEMS) fabrication methods to fabricate silicon microbarbs. There is a need for alternative fabrication methods that can shape microbarbs out of a broader range of materials, including polymers and metals.

An emerging micro-manufacturing technique, *micro-milling*, can be used to fabricate micro-scale piercing-element based mechanical attachment components from biocompatible materials [19–23]. Micromilling uses micro-scale milling tools (as small as $10 \mu m$ in diameter) within high-precision CNC or miniature machine tool (MMT) platforms. Increased throughput is realized by the use of ultra-high-speed spindles.

The micromilling process is markedly different from its macro-scale counterpart due to the scaling effects [20,22]. As illustrated in Fig. 1, the edge and corner radii of the commercially available tungsten carbide micro-endmills are in the order of a few micrometers [23]. Due to the flexibility and fragility of the micro-scale tools, the feed values during micromilling cannot exceed a few micrometers. Therefore, the edge and corner radii of the micro-endmills are commensurate with the feed values (uncut chip thicknesses) utilized during micromilling.

The large cutting-edge radius (bluntness) induce peculiar effects, causing erratic force variations, large forces, tool breakage, poor surface finish, and extensive burr formation [22–24]. The process becomes ploughing (rather than shearing) dominated, in which a large portion of the material is deformed and pushed under the tool. The elastic portion of this deformation recovers after the tool passes. Below a certain chip thickness, usually referred to as the *minimum chip thickness*, no chip is produced, and the entire material is pushed under the tool [20]. The mechanical behavior of the material is also altered due to the well-known size effect.

In addition to the changes in process mechanics, process kinematics of micromilling also differ significantly from those of conventional milling. During micromilling, the tool tip runout arising from the spindle-axis offset and tool tilt could be as large as the feed rate. As a result, the effective feed rate on each flute varies considerably. This variation can reach high enough levels to cause some of the teeth not to remove any material during the entire process [25]. Effective fabrication of micro-scale medical attachment components through micromilling cannot be realized without a thorough study on the effects of cutting conditions on forces, geometry, surface finish, and burr formation.

In this paper, the feasibility of micromilling to fabricate micro-scale mechanical attachment components is investigated. The particular attachment components considered here are referred to as *microbarbs*, which include a sharp piercing edge and a re-entrant feature obtained by undercutting. For each of the two types of tools required for the microbarb fabrication, a design of experiments study is conducted on a biocompatible polymer polymethyl methacrylate (PMMA) to investigate the effects of cutting conditions (feed, speed, and depth of cut) on micromilling forces, surface roughness, and burr formation. The geometric capability of the process is illustrated by fabricating PMMA microbarbs with different geometric characteristics. To demonstrate the material capability, microbarbs are also created from other biocompatible materials, including a bioresorbable material polylactic acid (PLA) and fibrin-based plastics, and a non-bioresorbable 304 stainless steel.

2. Fabrication of microbarbs

This section describes the design requirements and characteristics of microbarbs for medical implant applications. Also presented in this section are the geometry of the particular (custom) micro-endmills utilized for microbarb fabrication and the process plan used during micromilling.
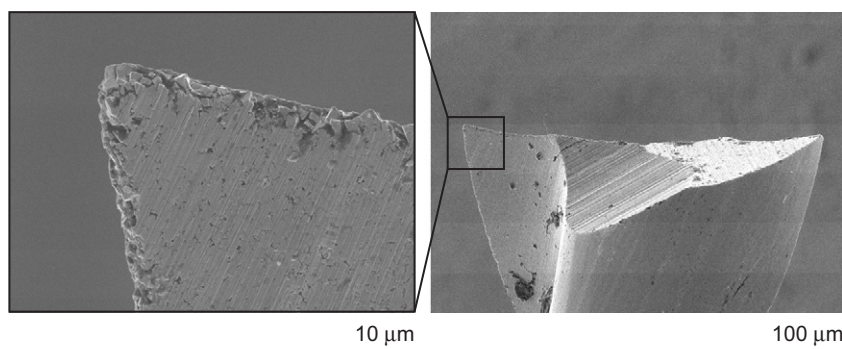

10 µm   100 µm

Fig. 1. An unused two-fluted tungsten carbide micro-endmill with $254 \mu m$ diameter. The serration and voids along the cutting edges, as well as the large edge and corner radii are visible.

2.1. Microbarb design

To be effective, a medical attachment component must satisfy geometric, mechanical-strength, and bio-compatibility requirements. In order to minimize the attachment force and tissue damage during the insertion, each piercing element is required to be small and to possess a sharp edge. To provide a secure and reliable attachment, re-entrant features that resist detachment must be present. For compatibility with human body, the attachment components must be manufactured from biocompatible materials. Further requirements include smooth and burr-free surfaces.

The geometry of the mechanical attachment components considered in this study, referred to here as *microbarbs*, is illustrated in Fig. 2. This design fulfills the aforementioned geometric and mechanical-strength requirements. Each microbarb is characterized by a sharp tip that facilitates the piercing, and an undercut as a re-entrant feature. The tip sharpness is controlled by the included angle of the head. The support angle between the stem and the head determines the strength of the microbarb against detachment and failure. The width and height of the head and stem can be varied according to the application requirements. The barb spacing can also be varied depending on the particular application to control the piercing forces and the overall strength of the attachment.

2.2. Process planning

Fabrication of the microbarbs with the proposed design necessitates the use of tools that can create the undercuts and the inclined surfaces, which will form the microbarb heads. The microbarb geometry can be created by sequentially using a V-shaped and an inverted T-shaped tools. As illustrated in Figs. 3(a) and (b), V-channel arrays are micromilled in two mutually perpendicular directions to produce micro-pyramids. This is followed by T-slot micromilling along the same two directions, as seen in Figs. 3(c) and (d) to obtain an array of microbarbs.

The V- and T-shaped micro-endmills used during this investigation are presented in Fig. 4. The V-shaped tool is a two-fluted endmill with a 90° included angle and straight

(zero helix angle) cutting edges. The tip of the tool has an approximately 40 μm wide chisel-like edge. The overall geometry of the V-shaped tool resembles other micro-endmills, with a 3.125 mm tool shank that tapers down to the final diameter.

The T-shaped tool, which is a two-fluted micro-endmill, has cutting edges only at the very end, and then the tool diameter reduces abruptly to allow undercutting. Unlike the V-shaped tool, the T-shaped tool was not commercially available. The authors fabricated this tool using a 344 nm Nd:YAG UV laser on a New Wave Research LaserMill®. A commercial micro-endmill with 254 μm diameter was attached to a fixture with two miniature bearings. The laser was used to selectively remove the material from the tool periphery where the smaller diameter is required. The laser was set to the UV-wavelength output and was pulsed at 50 Hz. The laser beam was masked to remove material only within a square-shaped 60 μm × 60 μm area. The duty cycle was set to 70%, and the fluence of the laser was selected to be 7 J/cm^2. The tool was rotated a small angle after every 10 seconds of exposure to create a cylindrical stem. Careful observation under a scanning electron microscope (SEM) indicated that the laser removal did not induce any measurable damage to cutting edges. Some re-deposited material was observed on the undercut region and on the periphery of the tool.

In order to manufacture two different sizes of micro-barbs, two T-shaped tools with different sizes (shown in Fig. 5) were fabricated. The larger T-shaped tool had 254 μm diameter and 80 μm axial (fluted) depth, while the smaller T-shaped tool had 101.6 μm diameter and 40 μm axial depth. The diameters of these tools defined the minimum separation between the stems of two adjacent microbarbs, whereas the axial fluted depths defined the minimum stem height.

The undercutting angle of the T-shaped tool is critical for the performance of the microbarbs. In this work, undercutting angles in the vicinity of 90° are considered to strike a trade-off between the strength against breakage and the resistance against detachment. Since the cutting edges are located only along the periphery, when the T-shaped micro-endmills with undercutting angles larger than 90° are used, considerable amount of rubbing and ploughing can occur on the undercut region. Such rubbing and ploughing can cause increased forces and burr
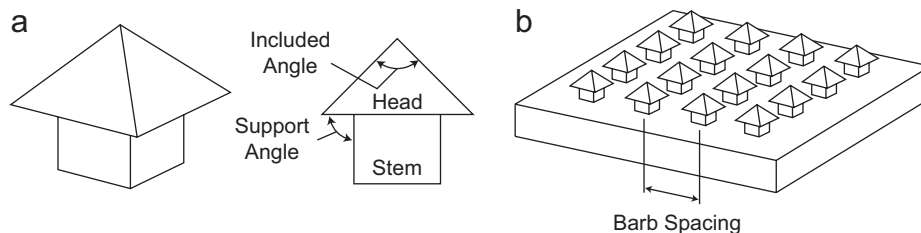

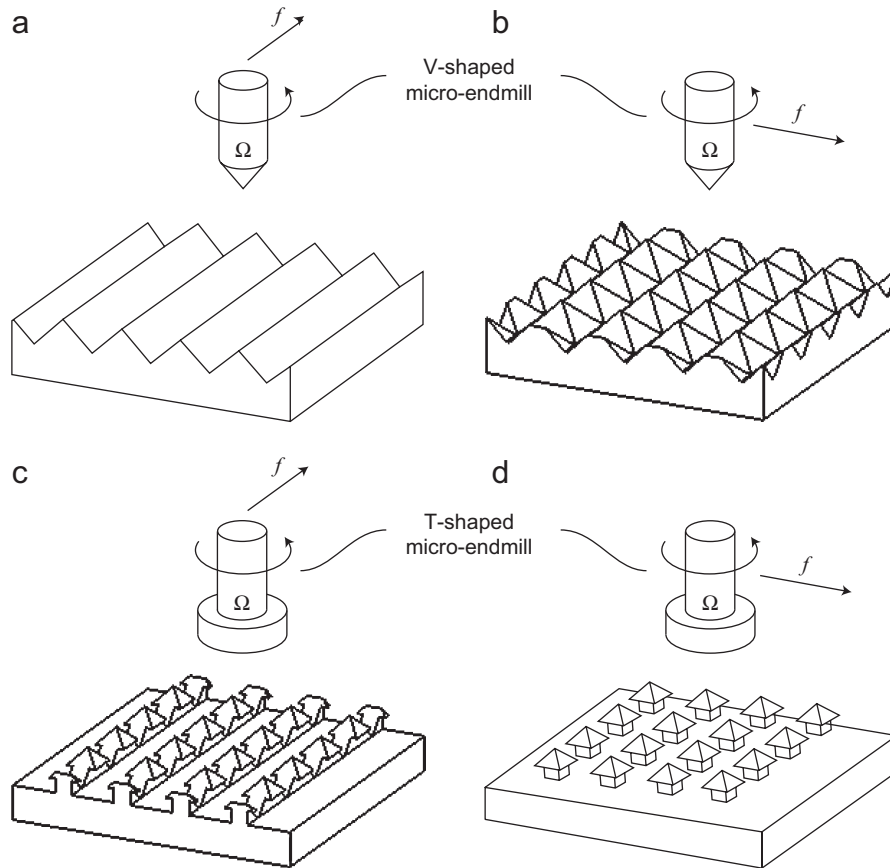Fig. 2. Geometry of (a) a single microbarb and (b) an array of microbarbs.

Fig. 3. The process steps for the creation of microbarbs: (a) the use of the V-shaped micro-endmill to create the V-channels, (b) creation of the micropyramids by feeding the V-shaped tool perpendicular to the feeding direction during the previous step, (c) the use of the T-shaped tool for the first undercutting, and (d) creation of the microbarbs by feeding the T-shaped tool perpendicular to feed at the previous step.
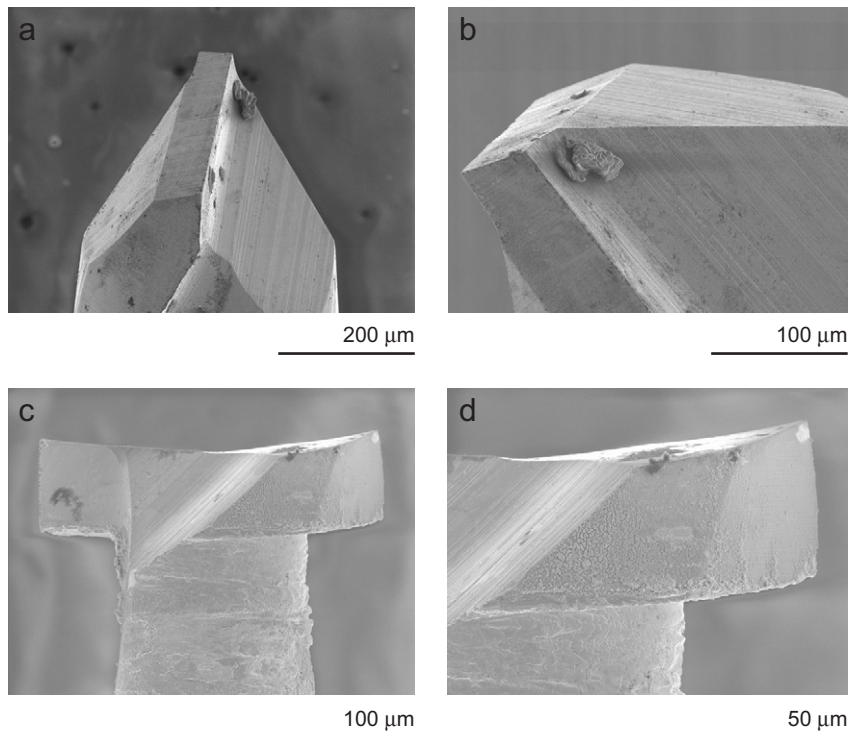

Fig. 4. (a) The V-shaped micro-endmill with 40 μm chisel-like edge, (b) a close-up view of the V-shaped micro-endmill, (c) the T-shaped micro-endmill with 254 μm tool diameter, and (d) a close-up view of the T-shaped micro-endmill.
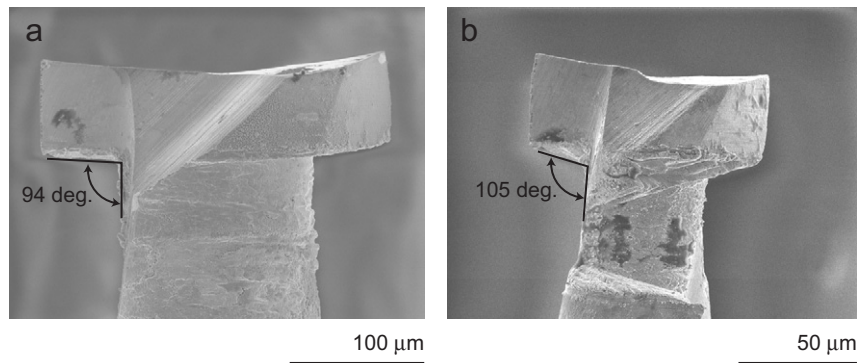
Fig. 5. (a) The T-shaped micro-endmill with 254 μm diameter and 80 μm fluted axial depth, (b) the smaller T-shaped micro-endmill with 101.6 μm diameter and 40 μm fluted axial depth.

formation. The undercutting angle of the larger T-shaped tool was estimated to be 94°, whereas the undercutting angle of the smaller T-shaped tool was seen to be approximately 105° (Fig. 5). The larger undercutting angle of the smaller tool is caused by the lack of more precise masking capability of the lasermill.

3. Experimental setup and methodology

This section describes the facility utilized to conduct the experimentation presented in this work. The experimental methodology, including the experimental conditions and the approach used for measuring various parameters, is also described in this section.

3.1. Experimental facility

The experimental studies presented here were completed using a high-precision miniature machine tool (MMT) shown in Fig. 6. The MMT has a 160,000 rpm air-turbine, air bearing spindle with a 3.125 mm (1/8 in) precision collet. A three-axis Aerotech ALS130-XYZ slide with 10 nm resolution, 250 mm/s maximum linear (feed) speed, and 25 mm × 50 mm × 50 mm workspace was used to provide the feeding motions. The control of slide motion was performed using a standard G-code programming. A Kistler® three-axis dynamometer (9256C1) with 2 mN noise threshold was attached to the slides for measuring the micromachining forces. A stereo microscope with 95X magnification is used to view the process and to indicate the workpiece surface during the initial tool approach.

3.2. Experimental methodology

As previously described, micromilling of microbarbs necessitate the use of two types of microtools, including the V-shaped and T-shaped micro-endmills. For each of these tools, design of experiments studies were performed to assess the effect of process parameters (feed, speed, and axial depth of cut) on the micromilling forces, surface finish, and burr formation. This section presents the methodology used for each of the experiments, including
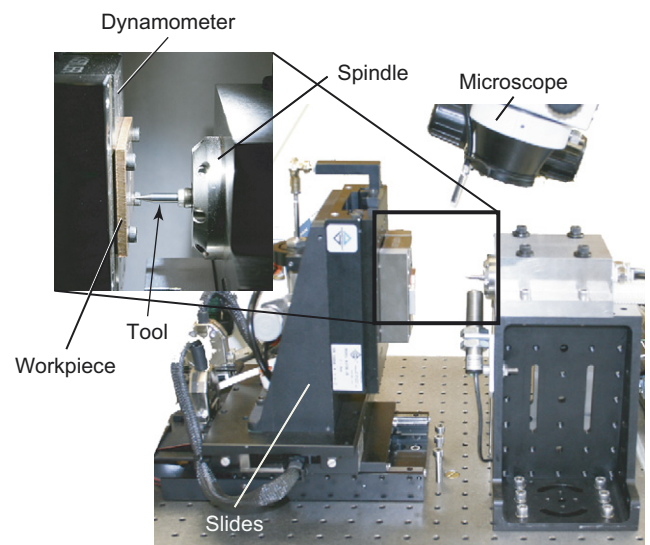

Fig. 6. The miniature machine tool (MMT) used during the experimentation.

the experimental conditions and measurement of micromilling forces, surface roughness, and burr formation.

3.2.1. Micromilling forces

A representative set of micromilling forces (V-channel micromilling, 5 μm/flute feed, 50 krpm spindle speed, and 10 μm depth of cut) is given in Fig. 7. The dashed lines indicate revolutions of the tool (with an arbitrary starting angle). Fig. 8 illustrates the orientation of the feed force F_y and the normal force F_x. The previously mentioned effects of large tool-tip runout, minimum chip thickness, elastic recovery, and ploughing-dominated process are reflected in the force signature. As a result, micromilling forces do not exhibit the one-per-revolution periodicity expected from the kinematics of the process.

To investigate the effects of feed, speed, and axial depth of cut on the performance of the V-shaped tools, a design of experiments study was conducted on PMMA. The investigation included a 2^3 full-factorial design of experiments with two spindle speeds (50, 100 krpm), two feeds (1, 5 μm/flute), and two axial depths of cut (10, 20 μm).

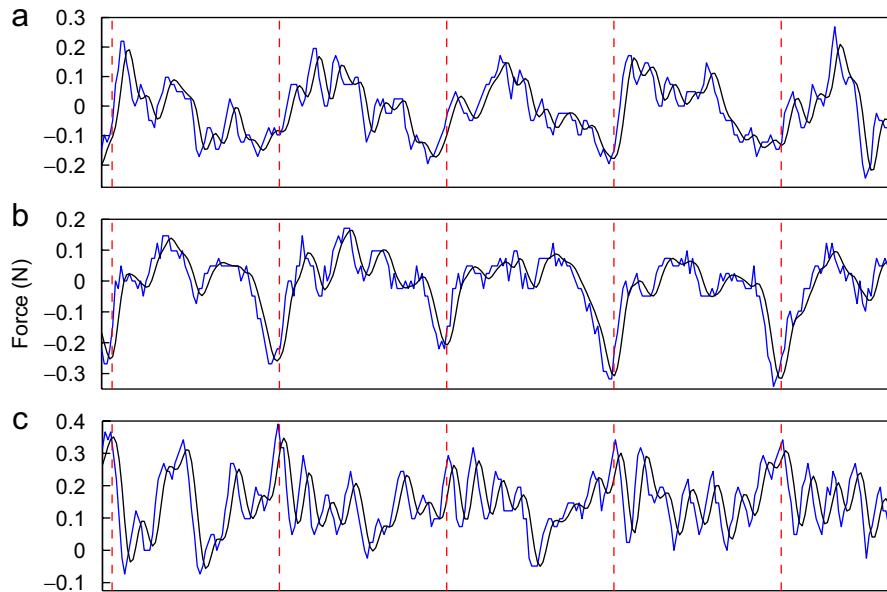Fig. 7. Sample micromilling forces in the (a) normal (x), (b) feed (y), and (c) axial (z) directions (5 μm/flute feed, 50 krpm spindle speed and 10 μm depth of cut).
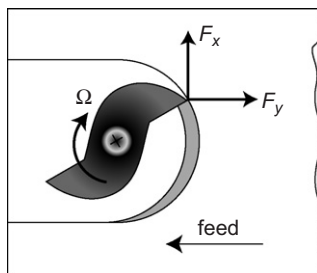

Fig. 8. Orientation of the micromilling forces.
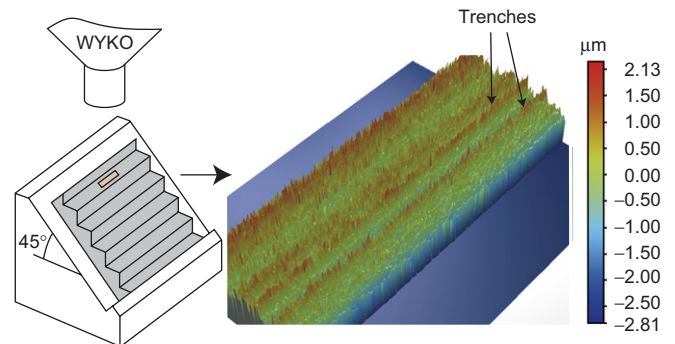

Fig. 9. The configuration of surface roughness measurements for the V-channels, and a sample image from the white-light interferometer (for 50 krpm spindle speed, 1 μm feed and 10 μm depth of cut).

The data was collected from cuts performed on previously fabricated V-channels. To assess the repeatability and to obtain independent error estimates, each experiment was conducted twice. The experimental results were analyzed through analysis of variance (ANOVA) approach considering the peak-to-valley (P-to-V) forces in each of the feed, normal and axial directions as the response parameters. In each case an average P-to-V force was calculated by averaging P-to-V force over the number of revolutions for a channel length of 0.75 mm.

Similarly, an ANOVA analysis was performed for micromilling with the *T-shaped tools* (using the larger T-tool shown in Fig. 5) on PMMA. In this case, a 2^2 full-factorial design of experiments with two spindle speeds (50, 100 krpm), and two feeds (1, 5 μm/flute) was performed. The axial depth of cut was not varied in this study since the entire fluted region of the T-tool is used. To ensure that the analysis applies to the cutting configuration used for microbarb fabrication, a set of V-channels were fabricated prior to cutting with the T-shaped tool, and the data was collected when undercutting the V-channels. Each

test was replicated twice to assess the repeatability and to obtain an independent error estimate.

3.2.2. Surface roughness

To assess the effect of the process parameters on surface roughness, the surface roughness (in terms of the average roughness R_a) was measured using a white-light interferometer (WYKO®) with vertical-scanning interferometry (VSI) mode and a 10X microscope objective (a total of 20X magnification). Since the main interest here is the roughness of the inclined features that form the microbarb heads, the surface roughness was analyzed only for the V-tool micromilling. Because WYKO® is only capable of measuring surfaces perpendicular to its optical measurement axis, the V-channels were tilted by 45°, as shown in Fig. 9 to orient the surfaces for measurement. To obtain proper reflectivity, the surfaces were coated with a layer of

gold with less than 5 nm thickness. Areal measurements capturing the entire field of view were separately taken from the beginning, middle and end sections of each channel, and were averaged to obtain an average surface roughness value. To enable assessing the repeatability, the measurements were conducted on two separate channels created using the same set of micromachining parameters.

3.2.3. Burr formation

To examine the effect of process parameters on the formation of burrs, burr charts were composed using the SEM images of the machined features. Each burr chart (one for the V-shaped and another for the T-shaped tools) is a table with the feed rates and speeds used for micromilling in the horizontal and vertical axis of the table, respectively. The individual cells of the table include the SEM image of the top of the channels for the particular process parameters. The use of the burr charts allowed a qualitative assessment of the effect of process parameters on burr formation. Additional experiments at an intermediate level of feed rate (3 μm/flute) were conducted to further facilitate the qualitative assessment. In the case of the V-tool micromilling, two burr charts for the two axial depth of cut were merged into a larger burr chart.

4. Results and discussion

This section presents the experimental results and the associated discussion. First, the results and discussion for the V-shaped tool is presented. This is followed by the results and discussion for the T-shaped tool.

4.1. Micromilling with the V-shaped tool

In this section, the experimental results on the *V-shaped tool* micromilling are outlined. Each response parameter (micromilling forces, surface roughness, and burr formation) is separately considered below.

4.1.1. Micromilling forces for V-tool micromilling

An ANOVA analysis was conducted to assess the effect of each parameter and to obtain an independent error estimate for the experimentation. The construction of the ANOVA table is illustrated in Table 1 considering the P-to-V normal forces. The calculated F-value for any of the main or interaction effects being larger than that of the F-value for a 95% confidence band ($F_{(1,8,0.95)} = 5.32$) indicates that the observed change arises from the change in the effects rather than the variation due to replications [26]. In that case, the effect is considered to be statistically significant. The F-value of the mean being larger than $F_{(1,8,0.95)}$ indicates that the variances are around a non-zero mean value.

The F-value columns for the normal, feed, and axial forces are compiled in Table 2. Although complete modeling of the micromilling process with V-shaped tool is beyond the scope of the present text, when interpreting

Table 1
The ANOVA table for the P-to-V normal forces for V-channel machining

Sources of variation	Sum of squares	DOF	Mean square	F-value
Mean	10.248	1	10.248	**6849.98**
E_1 (feed)	0.003	1	0.003	1.90
E_2 (speed)	0.272	1	0.272	**181.61**
E_3 (depth)	0.013	1	0.012	**8.20**
E_{12}	0.004	1	0.004	2.59
E_{13}	0.001	1	0.001	0.76
E_{23}	0.003	1	0.003	1.86
E_{123}	0.003	1	0.003	2.00
Pure error	0.012	8	0.001	
Total	10.558	16		

Statistically significant F-values are indicated using bold typeface

Table 2
The F-values of the micromilling forces in normal, feed, and axial directions during V-channel machining

F-values	X-normal	Y-feed	Z-axial
Mean	**6849.98**	**4418.29**	**5550.89**
E_1 (feed)	1.90	**89.78**	**6.13**
E_2 (speed)	**181.61**	**60.56**	**150.02**
E_3 (depth)	**8.20**	**14.05**	2.04
E_{12}	2.59	**7.16**	0.13
E_{13}	0.76	0.01	0.46
E_{23}	1.86	0.05	0.93
E_{123}	2.00	0.37	2.11

the results of the analysis, the particular geometry and kinematics of the V-shaped tool (see Fig. 4) must be considered. In addition to the 45° cutting edges, the large chisel-like edge also removes material. Due to the large negative rake angles, the forces arising from the chisel-like edge can be as high as those from the cutting edges. The chisel-like edge also causes cutting angles (oblique and rake angles) and cutting speed to vary along the straight cutting edges. Overall, micromilling with the V-shaped tool produced less than 1 N force magnitude.

For the average P-to-V *normal* forces, the main effects of the speed and depth of cut were seen to be statistically significant. These effects are represented in the main effect plots given in Fig. 10, which indicates that an increase in either the spindle speed or the axial depth of cut causes an increase in average P-to-V normal forces. The increase in average P-to-V normal forces may be explained by considering the strain-rate dependent behavior of the PMMA [27]. Although the P-to-V forces increase with increased depth of cut, this increase seems to be smaller than that expected from kinematic considerations. It is possible that the large forces from the chisel-like edge are independent of the axial depth of cut, causing an offset in the P-to-V forces.

For the P-to-V *feed* forces, the main effects of feed rate, spindle speed and axial depth of cut, as well as the interaction effects between the feed rate and spindle speed
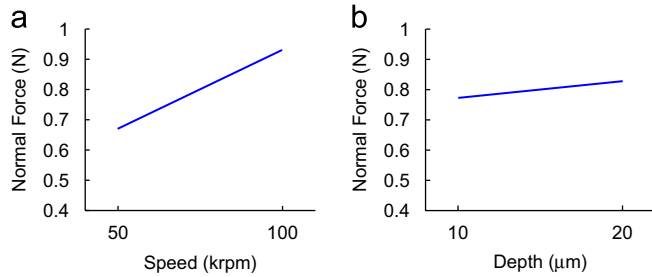
Fig. 10. The main effects of (a) speed, and (b) depth of cut on the normal forces during V-channel micromachining.
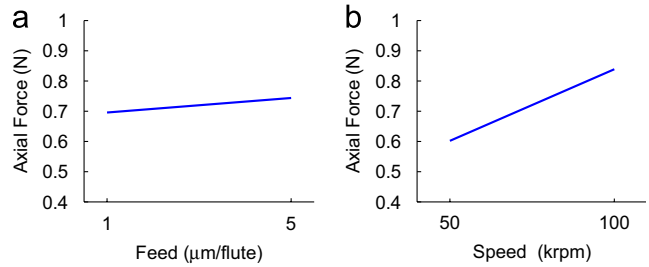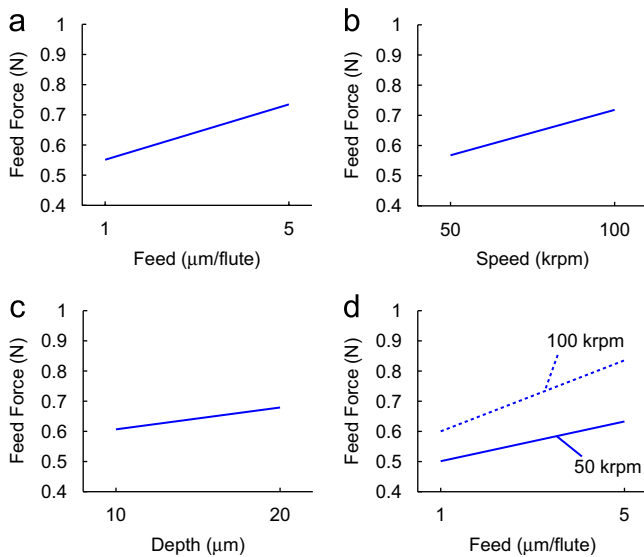

Fig. 11. The main effects of (a) feed, (b) speed, (c) depth of cut, and (d) the interaction effect of feed and speed; on the feed forces during V-channel micromachining.

Fig. 12. The main effects of (a) feed and (b) speed on the axial forces during V-channel micromachining.

Table 3
The ANOVA table for the V-channels surface roughness (R_a)

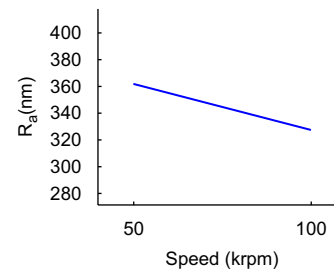| Sources of variation	Sum of squares	DOF	Mean square	F-value
Mean	1 900 903.3	1	1 900 903.3	**18 115.8**
E_1 (feed)	72.5	1	72.5	0.7
E_2 (speed)	4744.1	1	4744.1	**45.2**
E_3 (depth)	67.4	1	67.4	0.6
E_{12}	30.1	1	30.1	0.3
E_{13}	7.6	1	7.6	0.1
E_{23}	329.7	1	329.7	3.1
E_{123}	386.0	1	386.0	3.7
Pure error	839.4	8	104.9	
Total	1 907 380.2	16		

Fig. 13. The main effect of spindle speed on the V-channel surface roughness (R_a).

were seen to be statistically significant. Figs. 11(a) and (b) illustrates these effects. It was seen that an increase in spindle speed, feed, and depth of cut caused an increase in P-to-V feed forces.

For the average P-to-V *axial* force, the main effects of feed and speed are found to be statistically significant. From the main effects given in Fig. 12, it is observed that the axial force increased with increasing feed and speed, the latter of which had a higher effect. The axial forces arise from the 45° angle of the cutting edges, the oblique cutting action, and the forces from the chisel-like edge.

4.1.2. Surface roughness from V-tool micromilling

The roughness of the surfaces created by the V-shaped tool were also analyzed through an ANOVA analysis. Table 3 gives the ANOVA table for the V-channel surface roughness in terms of the average surface roughness R_a. Comparison of the F values with $F_{(1,8,0.95)} = 5.32$ indicated that only the main effect of spindle speed was statistically significant within the ranges of parameters considered during the experimentation. The main effect of spindle speed is plotted in Fig. 13, which shows that surface

roughness reduces from 360 to 320 nm when the spindle speed is increased from 50 to 100 krpm. A number of trench-like features, similar to those seen in Fig. 9, were observed in every measurement. The serration of the cutting edges and/or cutting edge irregularities such as notches, are considered as possible causes of the trench-like features. It is possible that these trench-like features cause larger surface roughness values than those arising from changes in the micromilling parameters. Since the main effects of axial depth of cut and feed rate, as well as all the interaction effects, are statistically insignificant, the throughput of the process can be increased significantly without compromising the surface roughness.

4.1.3. Burr formation during V-tool micromilling

The burr chart for the V-shaped tools is given in Fig. 14. An examination of the burr chart indicates that, for the
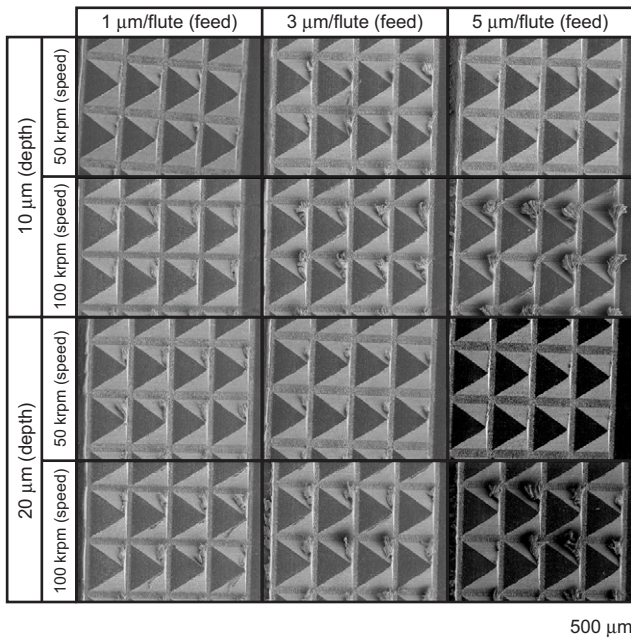
Fig. 14. A burr chart showing the micro-pyramids fabricated by the V-shaped tool under different conditions.

Table 4
The F-values of the micromilling forces in normal, feed, and axial directions during T-channel machining

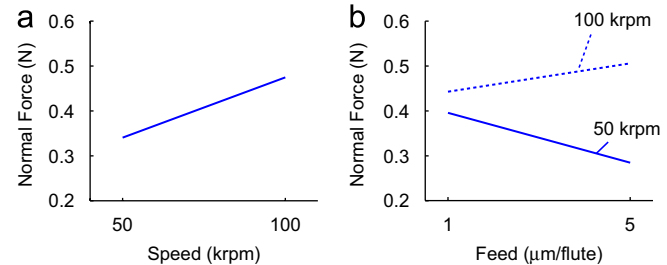| F-values	X-normal	Y-feed	Z-axial
Mean	**1312.70**	**25 146.01**	**4295.21**
E_1 (feed)	1.14	**718.66**	**33.41**
E_2 (speed)	**35.49**	**724.76**	**332.73**
E_{12}	**14.96**	**214.72**	7.42

Fig. 15. (a) The main effects of speed and (b) the interaction effect of feed and speed on the normal forces during T-channel micromachining.

higher speed of 100 krpm, the burr formation increases with increasing feed for both axial depth-of-cut levels. Although the effect of axial depth of cut was small, the lower depth of cut of 10 µm produced more burrs. The most extensive burr formation was seen for the condition with the higher depth of cut (20 µm), the higher speed (100 krpm), and the highest feed (5 µm/flute). The least amount of burr formation (no visible burrs) was seen for the conditions with the higher depth of cut (20 µm), the lower speed (50 krpm), and the highest feed (5 µm/flute).

4.2. Micromilling with the T-shaped tool

This section presents the experimental results for the *T-shaped tool* micromilling. The effect of process parameters on micromilling forces and burr formation are considered below. As stated previously, the roughness of the surface created by the T-shaped tools are not analyzed in this work since they do not affect the performance of the microbarbs.

4.2.1. Micromilling forces for T-tool micromilling

An ANOVA analysis, similar to that for the V-shaped tools, was conducted for the T-shaped tools. Table 4 gives the F-value columns of the ANOVA table for the average P-to-V normal, feed, and axial forces. The average P-to-V forces were calculated by averaging the P-to-V force from the number of revolutions in approximately 0.75 mm cutting length. The F values were compared to $F_{(1,4,0.95)} = 7.71$ to decide the statistical significance of an effect. It is seen that the mean values for each force was statistically significant, indicating that the variations in P-to-V forces

were around a nonzero value. Overall, the P-to-V T-channel forces were within 0.3–0.55 N.

In interpreting the analysis results, the geometry and kinematics of the cutting process with the T-shaped tool must be considered. The undercutting angle of the T-shaped tool being greater than 90° causes rubbing on the undercut region of the microbarb heads. In addition, since the cutting was preformed after the V-channels were made, the cutting edges of the T-shaped tool did not encounter any material along the center of the channels.

For the P-to-V normal forces, the main effect of speed and the interaction effect of speed and feed were seen to be statistically significant. These effects are plotted in Fig. 15. The forces were seen to increase with increasing speed. The interaction effect revealed that while the forces increase with increasing feed rate for the higher speed of 100 krpm, they decrease with the increasing feed rate for 50 krpm.

For the P-to-V feed forces, the main effects of the feed and speed, and the interaction effects of the feed and speed, were seen to be statistically significant. Fig. 16 indicates that increase in either feed rate or spindle speed causes increased P-to-V feed forces. The effect of feed rate is less for the lower spindle speed of 50 krpm.

For the P-to-V axial forces, only the main effects of feed and speed were statistically significant. The main effect plots in Fig. 17 indicate that the axial forces increase with increasing feed rate or increasing speed. The effect of speed was more prominent. The large magnitude of axial forces possibly arise from the rubbing action on the undercut region of the microbarb heads.

4.2.2. Burr formation during V-tool micromilling

Fig. 18 presents the burr chart composed for qualitative analysis of burr formation in T-tool micromilling. It can be
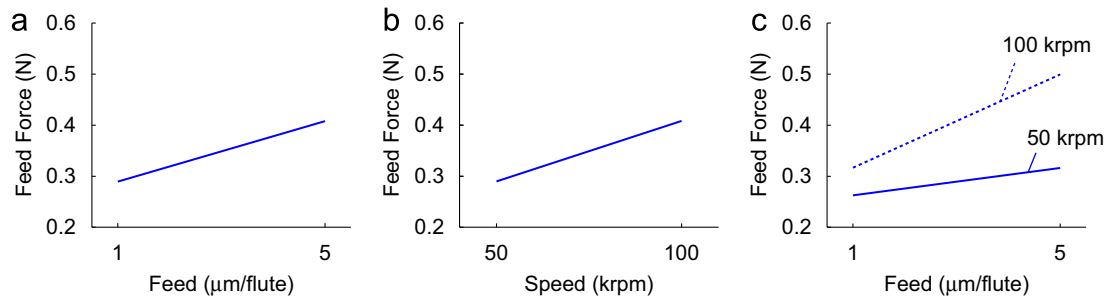
Fig. 16. The main effects of (a) feed and (b) speed, and (b) the interaction effect of feed and speed; on the feed forces during T-channel micromachining.
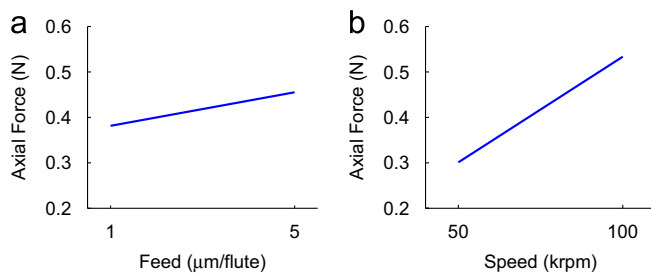

Fig. 17. The main effects of (a) feed and (b) speed on the axial forces during T-channel micromachining.
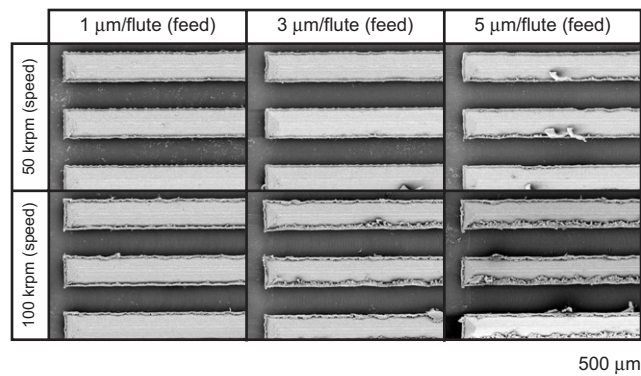

Fig. 18. A burr chart showing the T-channels fabricated by T-shaped tool under different conditions.

observed from the burr chart that increasing feed rate caused increased burr formation for both spindle speeds. The effect of feed was considerably more prominent at the higher spindle speed of 100 krpm. The lowest burr formation was observed for the lowest feed rate of 1 μm/flute and the lower speed of 50 krpm.

5. Geometric and material capability

In this section, the geometric and material capabilities of the micromilling process in fabricating microbarbs are demonstrated. These capabilities are important since different implant applications call for different geometries and materials.

5.1. Geometric capability

To be effective, the micro-manufacturing technique used in fabrication of the microbars should be capable of creating a range of geometries for different attachment applications. In this section, the basic geometric capability of the micromilling process in terms of producing different microbarb sizes, stem heights, and included angles (sharpness) is demonstrated.

Fig. 19 illustrates SEM images of an individual PMMA microbarb and an associated array of microbarbs. These microbarbs have a stem width of 100 μm, a stem height of 80 μm, a head width of 174 μm, and an overall height of 167 μm. The barb separation of the microbarb array is 304 μm. During the fabrication, a set of conditions that resulted in minimal burr formation in the above study were used (50 krpm spindle speed, 20 μm axial depth of cut, and 5 μm/flute feed for the V-shaped tool; 50 krpm spindle speed, 1 μm/flute feed for the T-shaped tool). To remove the small amount of burrs caused by the T-shaped tool, a finishing pass with 5 μm axial depth of cut was performed with the V-shaped tool using 50 krpm spindle speed and 5 μm/flute feed rate. The support angle of the microbarb in Fig. 19(b) was estimated to be approximately 90°.

To demonstrate the capability of micromilling in producing different microbarb sizes, a set of smaller PMMA microbarbs with a stem width of 40 μm, a stem height of 50 μm, a head width of 68 μm, an overall height of 84 μm were created. Fig. 20 shows the SEM images of the smaller microbarbs and an associated array of microbarbs, which has a barb separation of 122 μm. While the same V-shaped tool was used for creating the microbarb heads as for the larger microbarbs, the undercutting of the smaller microbarbs was performed using the smaller T-shaped tool (Fig. 5(b)). The surface roughnesses of these microbarbs were comparable to those of the larger microbarbs, although the higher image magnification in Fig. 20(a) causes the surfaces appear rougher. Fig. 20(b) also indicates relatively large burrs on the undercut sections of some of the small microbarbs. These burrs are caused by the material pushed by the large (approximately 104°) undercutting angle of the smaller T-shaped tool, and may be removed by performing a finishing pass using the T-shaped tool.
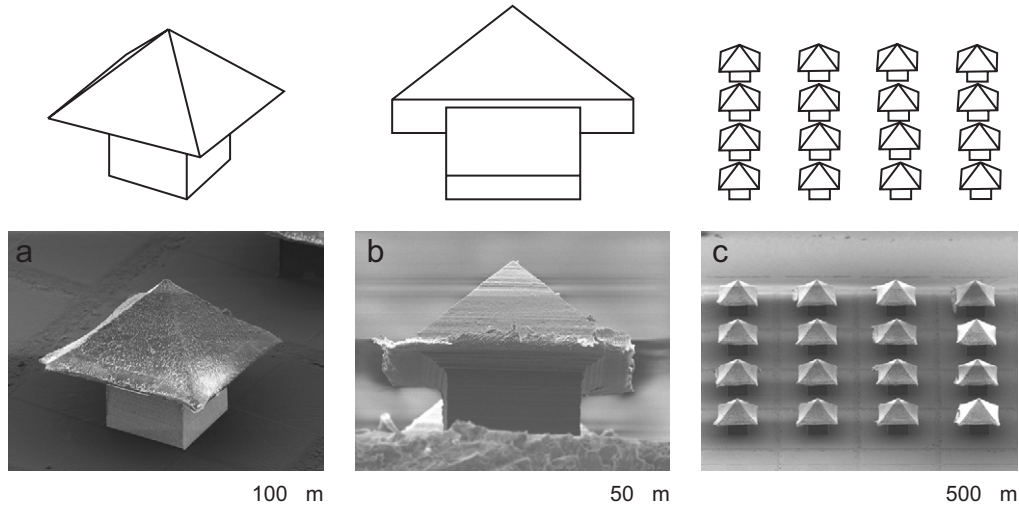
Fig. 19. (a) An SEM image of a PMMA microbarb, (b) another image of the microbarb showing the support angle, (c) an SEM image of a PMMA microbarb array.
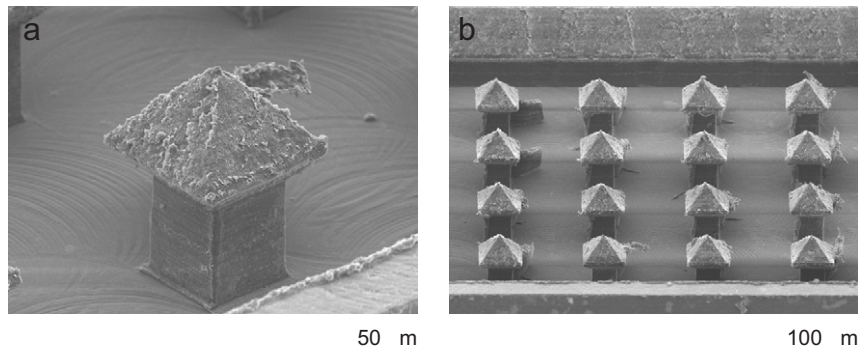

Fig. 20. (a) Microbarbs with smaller size (68 μm head width and 84 μm overall height), and (b) an array of smaller microbarbs.

The included angle (sharpness) of the microbarb heads can be varied by using a V-shaped tool with different included angle. The microbarbs illustrated previously had an included angle of 90°. To demonstrate the capability of creating different edge sharpnesses, a set of PPMA microbarbs with 60° included angle were fabricated. An individual 60° microbarb and associated array of microbarbs are shown in Figs. 21(a) and (b), respectively. These microbarbs have a stem width of 100 μm, a stem height of 100 μm, a head width of 185 μm, and an overall height of 260 μm. The barb separation for the array was 304 μm.

Since the stem height can be an important parameter for various applications, the capability of the micromilling process in creating different stem heights was also demonstrated. Microbarb arrays with stem heights of 200 μm (overall height of 360 μm) and 300 μm (overall height of 460 μm) are given in Fig. 21(c) and (d), respectively. Both arrays of microbarbs had an included angle of 60°, a stem width of 100 μm, a head width of 185 μm, and a microbarb separation of 304 μm. The longer stem heights were obtained by performing multiple passes with the T-shaped tool. The same micromilling conditions as those used for the larger microbarbs were used during micromilling these sharper microbarbs.

5.2. Material capability

In this section, the capability of the micromilling process to fabricate microbarbs from biocompatible materials, including non-degradable PMMA and 304 stainless steel, bioresorbable PLA, and fibrin-based bio-plastic [28] is investigated. Table 5 gives the micromilling parameters used during fabrication of the microbarbs for each material. It should be noted that the micromilling process was not investigated for materials other than PMMA, and therefore the micromilling conditions given in Table 5 reflect only a set of viable, rather than optimized, conditions. Furthermore, no finishing pass was performed during fabrication.

The micromilling conditions used for the fibrin microbarbs resembled those for the PMMA microbarbs. Use of similar conditions for the PLA microbarbs, however, caused the microbarbs to wrap around the tool and break during undercutting with the T-shaped tool. Therefore, the feed rate used for the T-shaped tool was considerably
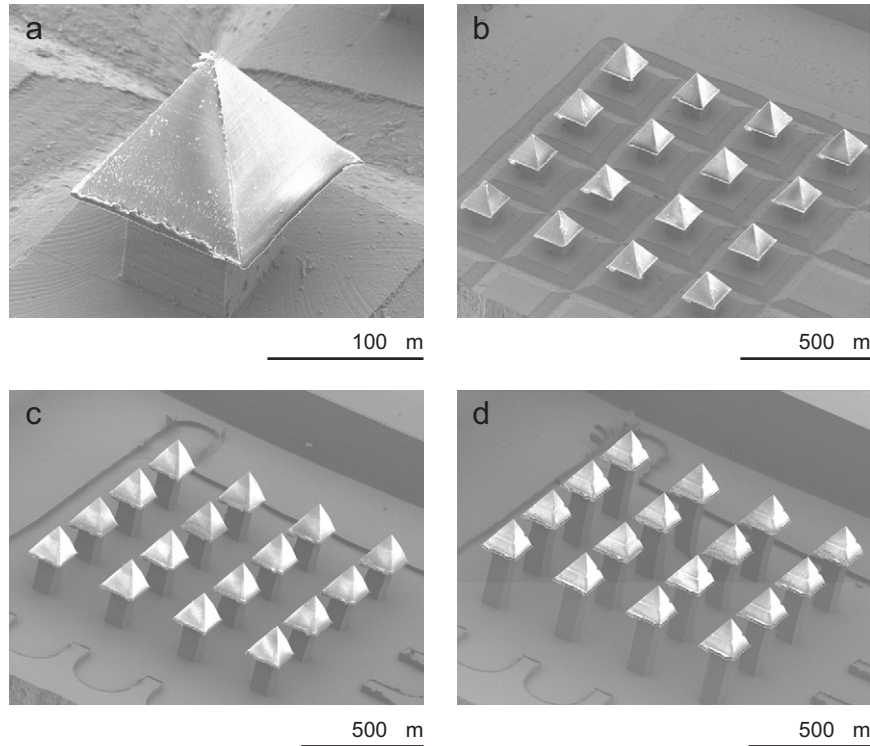
Fig. 21. (a) Microbarbs with 60° included angle, (b) a microbarb array with 60° included angle and 260 μm overall height, (c) a microbarb array with 360 μm overall height, and (d) a microbarb array with 460 μm overall height.

Table 5
Micromilling conditions used during fabrication of microbarbs from fibrin-based plastic, PLA, and 304 stainless steel (S/S 304)

Material	V-channels			T-channels	
	Spindle speed (krpm)	Feed (μm/flute)	Depth (μm)	Spindle speed (krpm)	Feed (μm/flute)
Fibrin	100	1	10	100	1
PLA	100	1	10	60	0.01
S/S 304	100	1	10	100	0.25

reduced to prevent breakage. Since preliminary testing on 304 stainless steel produced extensive tool wear and tool breakage (for T-shaped tool), coated tools with small feed rate were used for fabricating the stainless steel microbarbs. The use of TiAlN coated V-shaped tool and PCD coated T-shaped tool was sufficient to minimize the tool wear and eliminate the tool failure.

The resulting individual microbarbs and microbarb arrays are given in Fig. 22. It was seen that the overall geometry with the microbarbs were successfully created in all cases. The fibrin microbarbs (Figs. 22(a) and (b)) exhibited well-defined geometric features, with a small amount of burr formation on the microbarb heads, which may be removed by performing a finishing pass. The burr formation was more prominent for the PLA microbarbs (Figs. 22(c) and (d)), which is expected due to high ductility of the PLA. Again, a finishing pass may be conducted to

remove these burrs. Although the stainless steel microbarbs were not formed as well as those from the other materials, the microbarb heads and undercuts were still present. A considerable amount of smearing can be observed from the images in Figs. 22(e) and (f). This tendency of the stainless steel is well known from the conventional (macro-scale) milling operations [29].

6. Conclusions

This paper presented an investigation on the viability of micromilling for fabricating micro-scale piercing elements (microbarbs) from biocompatible materials that would be compatible for medical attachment applications. To determine the effect of micromilling conditions on micromilling forces, surface roughness, and burr formation, design of experiments studies and ANOVA analyses were performed on PMMA workpieces for V-shaped and T-shaped micro-endmills used during the microbarb fabrication. The capability of micromilling in creating different microbarb geometries was demonstrated by fabricating microbarbs with different sizes, included angles, and stem heights. The material capability of the process was demonstrated by fabricating microbarbs from biocompatible materials, including PMMA, PLA, fibrin-based plastic, and stainless steel. Since the micromilling process presented here lends itself to parallel production, the high production rate (large-scale production) critical for extensive application of microbarbs can be attained.
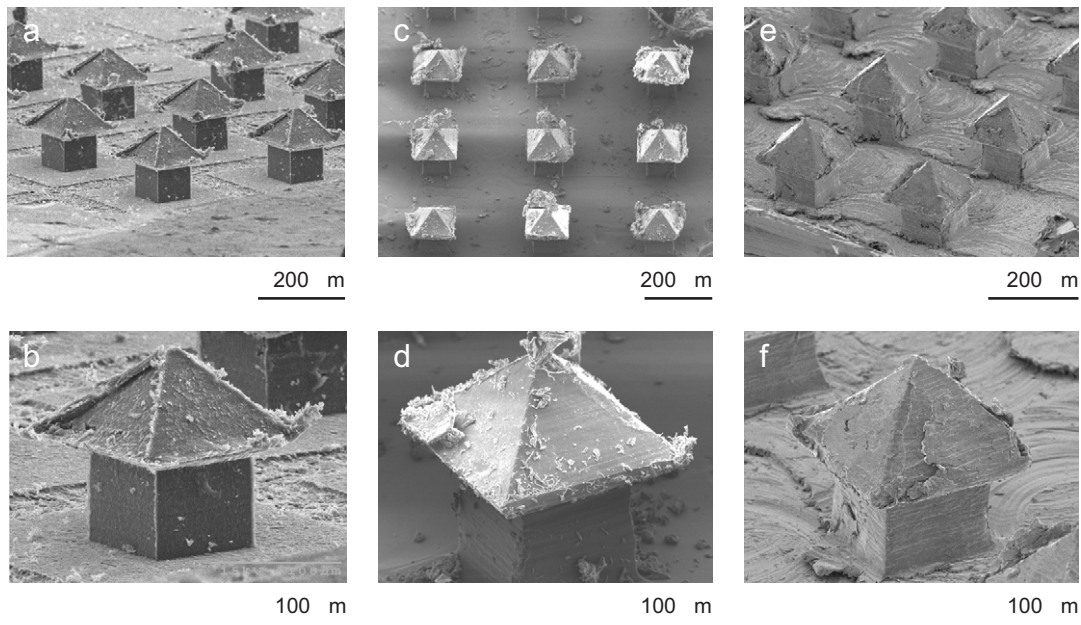
Fig. 22. (a) and (b) fibrin-based plastic microbarbs, (c) and (d) PLA microbarbs, (e) and (f) stainless steel microbarbs.

The following specific conclusions are drawn from the presented work:

- During the creation of PMMA microbarbs, the peak-to-valley forces in normal, feed and axial directions were below 1 N within for either of the V-shaped and T-shaped tools. The spindle speed was seen to have the most prominent effect for all force components, and increase in spindle speed was seen to cause an increase in forces.
- For the surface roughness of the PMMA V-channels, only the main effect of the spindle speed was statistically significant. This indicates the possibility of increasing the material removal rate without compromising on surface roughness.
- Sets of conditions that yield the lowest burr formation on PMMA for the V-shaped and T-shaped tools were identified through a quantitative analysis using a burr chart. The burr formation was shown to be minimized or completely eliminated with the use of proper micromilling conditions identified during the experimental investigation.
- By creating microbarbs with different sizes, sharper included angles, and higher stem heights, the micromilling process was shown to be capable of fabricating microbarbs with different geometries.
- It was shown that the micromilling process can be used to effectively create arrays of microbarbs on various biocompatible (permanent and bioresorbable) materials, including PMMA, PLA, fibrin-based plastic, and 304 stainless steel.

Acknowledgments

References

[1] J.D. Bronzino, The Biomedical Engineering Handbook, CRC Press, Boca Raton, 1995.
[2] J. Ouellette, Biomaterials facilitate medical breakthroughs, Industrial Physicist 7 (5) (2001) 18–21.
[3] D.A. LaVan, T. McGuire, R. Langer, Small-scale systems for in-vivo drug delivery, Nature Biotechnology 21 (10) (2003) 1184–1191.
[4] J.R. Davis, Handbook of Materials for Medical Devices, ASM International, 2003.
[5] B.D. Ratner, S.J. Bryant, Biomaterials: where we have been and where we are going, Annual Review of Biomedical Engineering 6 (2004) 41–75.
[6] H. Han, L. Weiss, M. Reed, Mating and piercing micromechanical structures for surface bonding applications, in: Proceedings. IEEE Micro Electro Mechanical Systems, An Investigation of Micro Structures, Sensors, Actuators, Machines and Robots, 1991, pp. 253–258.
[7] H. Han, L. Weiss, M. Reed, Micromechanical velcro, Journal of Microelectromechanical Systems (USA) 1 (1) (1992) 37–43.
[8] C. Flahiff, D. Feldman, R. Saltz, S. Huang, Mechanical properties of fibrin adhesives for blood vessel anastomosis, Journal of Biomedical Materials Research 26 (4) (1992) 481–491.
[9] M. Donkerwolcke, F. Burny, D. Muster, Tissues and bone adhesives—historical aspects, Biomaterials 19 (16) (1998) 1461–1466.

[10] H.J. Erli, R. Marx, O. Paar, F.U. Niethard, M. Weber, D.C. Wirtz, Surface pretreatments for medical application of adhesion, BioMedical Engineering OnLine (2003) 2–15.

[11] L. Xie, S.D. Brownridge, O.B. Ozdoganlar, L.E. Weiss, The viability of micromilling for manufacturing mechanical attachment components for medical applications, Transactions of the North American Manufacturing Research Institute of SME 34 (2006) 445–452.

[12] S. Byun, J.M. Lim, S. Paik, A. Lee, K.I. Koo, S. Park, J. Park, B.D. Choi, J.M. Seo, K.A. Kim, H. Chung, S.Y. Song, D. Jeon, D. Cho, Barbed micro-spikes for micro-scale biopsy, Journal of Micromechanics Microengineering (UK) 15 (6) (2005) 1279–1284.

[13] P. Griss, P. Enoksson, G. Stemme, Barbed spike arrays for mechanical chip attachment, Technical Digest. MEMS 2001, in: 14th IEEE International Conference on Micro Electro Mechanical Systems, 2001, pp. 46–49.

[14] M.L. Reed, H. Han, L.E. Weiss, Silicon micro-velcro, Advanced Materials 4 (1) (1992) 48–51.

[15] R. Prasad, K.F. Bohringer, N.C. MacDonald, Design, fabrication, and characterization of single crystal silicon latching snap fasteners for micro assembly, American Society of Mechanical Engineers, Dynamic Systems and Control Division (Publication) DSC, vol. 57(2), 1995, pp. 917–923.

[16] M. Turner, Adhesives: a selection guide, Medical Device Technology 10 (8) (1999) 29–33.

[17] S. Tavakoli, Adhesive bonding of medical and implantable devices, Medical Device Technology 13 (7) (2002) 32–36.

[18] S. Tavakoli, D. Pullen, S. Dunkerton, A review of adhesive bonding techniques for joining medical materials, Assembly Automation (UK) 25 (2) (2005) 100–105.

[19] G.L. Benavides, D.P. Adams, P. Yang, Meso-machining capabilities, Technical Report SAND2001-1708, Sandia National Laboratories, Albuquerque, New Mexico 87185 (June 2001).

[20] X. Liu, R.E. DeVor, S.G. Kapoor, K.F. Ehmann, The mechanics of machining at the microscale: assessment of the current state of the science, Transactions of the ASME, Journal of Manufacturing Science and Engineering 126 (2004) 666–678.

[21] T. Masuzawa, State of the art of micromachining, CIRP Annals—Manufacturing Technology 49 (2) (2000) 473–488.

[22] K. Ehmann, D. Bourell, M. Culpepper, R. DeVor, T. Hodgson, T. Kurfess, M. Madou, K. Rajurkar, WTEC Study on Micromanufacturing, 2005.

[23] S. Filiz, C. Conley, M. Wasserman, O.B. Ozdoganlar, An experimental investigation of micro-machinability of copper 101 using tungsten carbide micro-endmills, International Journal of Machine Tools and Manufacture, 2007, in press.

[24] K. Lee, D.A. Dornfeld, An experimental study on burr formation in micro milling aluminum and copper, Transactions of the NAMRI/ SME XXX (2002) 255–262.

[25] C. Kim, J. Mayor, J. Ni, A static model of chip formation in microscale milling, Transactions of the ASME, Journal of Manufacturing Science and Engineering 126 (2004) 710–718.

[26] D.C. Hoaglin, F. Mosteller, J.W. Tukey, Fundamentals of Exploratory Analysis of Variance, Wiley, New York, 1991.

[27] G. Palm, R. Dupaix, J. Castro, Large strain mechanical behavior of poly(methyl methacrylate) (PMMA) near the glass transition temperature, Journal of Engineering Materials and Technology 128 (2006) 559–563.

[28] M. Gerendas, in: K. Laki (Ed.), Fibrin Products as Aid in Hemostasis and Wound Healing, Fibrinogen, Marcel Dekker, New York, 1968, pp. 277–316.

[29] P. Wright, E. Trent, Metal Cutting, fourth ed., Butterworth-Heinemann, 2000.